Monthly Notices
of the
ROYAL ASTRONOMICAL SOCIETY

MNRAS **479,** 4878–4890 (2018)
Advance Access publication 2018 May 18

doi:10.1093/mnras/sty1314

On the evolution of vortices in massive protoplanetary discs

Arnaud Pierens[1,2] and Min-Kai Lin[3]

[1] *Université de Bordeaux, Observatoire Aquitain des Sciences de l'Univers, BP89 F-33271 Floirac Cedex, France*
[2] *CNRS, Laboratoire d'Astrophysique de Bordeaux, BP89 F-33271 Floirac Cedex, France*
[3] *Institute of Astronomy and Astrophysics, Academia Sinica, Taipei 10617, Taiwan*

Accepted 2018 May 14. Received 2018 May 9; in original form 2018 March 5

ABSTRACT

It is expected that a pressure bump can be formed at the inner edge of a dead zone, and where vortices can develop through the Rossby Wave Instability (RWI). It has been suggested that self-gravity can significantly affect the evolution of such vortices. We present the results of 2D hydrodynamical simulations of the evolution of vortices forming at a pressure bump in self-gravitating discs with Toomre parameter in the range 4−30. We consider isothermal plus non-isothermal disc models that employ either the classical β prescription or a more realistic treatment for cooling. The main aim is to investigate whether the condensating effect of self-gravity can stabilize vortices in sufficiently massive discs. We confirm that in isothermal disc models with $Q \gtrsim 15$, vortex decay occurs due to the vortex self-gravitational torque. For discs with $3 \lesssim Q \lesssim 7$, the vortex develops gravitational instabilities within its core and undergoes gravitational collapse, whereas more massive discs give rise to the formation of global eccentric modes. In non-isothermal discs with β cooling, the vortex maintains a turbulent core prior to undergoing gravitational collapse for $\beta \lesssim 0.1$, whereas it decays if $\beta \geq 1$. In models that incorporate both self-gravity and a better treatment for cooling, however, a stable vortex is formed with aspect ratio $\chi \sim 3$–4. Our results indicate that self-gravity significantly impacts the evolution of vortices forming in protoplanetary discs, although the thermodynamical structure of the vortex is equally important for determining its long-term dynamics.

Key words: accretion, accretion discs – hydrodynamics – methods: numerical – planets and satellites: formation.

1 INTRODUCTION

A striking feature of the current population of exoplanets is the broad diversity in system architectures that have been discovered. Among the known multiplanetary systems, a significant number consist of compact and non-resonant systems of Super-Earths and mini-Neptunes orbiting within a few tenths of au from their stars (Lissauer et al. 2011; Lovis et al. 2011). There are two basic scenarios for the formation of these systems. The first one corresponds to the *in situ* formation of these systems, involving planetesimal accretion within high-mass discs (Hansen & Murray 2012, Chiang & Laughlin 2013). This model however requires extremely massive protoplanetary discs with a broad range of surface density slopes, which is inconsistent with any known disc theory (Raymond & Cossou 2014). An alternative possibility is that systems of close-in Super-Earths formed through accretion during the inward migration of planetary embryos (Terquem & Papaloizou 2007; Ogihara & Ida 2009; Cossou et al. 2014). Super-Earths formed in this way are expected to migrate to the inner edge of the disc where they pile up in long chains of resonances. Resonant configurations can subsequently be broken during disc dissipation (Izidoro et al. 2017), or due to the action of disc turbulence (Pierens et al. 2011; Rein 2012) or interaction with planet wakes (Baruteau & Papaloizou 2013).

In the context of this model, understanding the physical conditions at the inner edge of the disc is therefore a crucial issue. In the very inner regions where temperatures are high enough for the disc to be thermally ionized, turbulence is expected to be driven by the magnetorotational instability (MRI) (Balbus & Hawley 1991). Beyond ∼0.8 au typically (Flock et al. 2017), however, temperature drop below the ionization threshold of alkali metals ($T \sim 1000$ K) prevents turbulence to be sustained, giving rise to the formation of a dead zone (Gammie 1996). Since magnetic stresses are order of magnitude weaker there, gas accretion is driven faster in the active region than in the dead zone. This results in the formation of a local maximum in the radial profile of the disc pressure, where dust particles can be collected and which can act as a planet trap (Masset et al. 2006). At this location, the recent 3D radiation MHD simulations of Flock et al. (2017) have also demonstrated that for realistic inner disc models, a vortex is likely to be formed through the Rossby Wave Instability (RWI) (Lovelace et al.

* E-mail: arnaud.pierens@u-bordeaux.fr

1999). Vortex formation through the RWI has also been invoked as a possible origin for the non-axisymmetric structures that have been observed in many transition discs, such as in Oph IRS 48 (van der Marel et al. 2013), or HD 142527 (Casassus et al. 2013; Fukagawa et al. 2013). In that case, the pressure maximum responsible for driving the RWI should be rather located at the outer edge of the dead zone where the disc transitions from low to high gas ionization where the MRI is active (Flock et al. 2017), or located at the edge of a planetary gap (Ataiee et al. 2013; Zhu et al. 2014).

Because of the reduction of the accretion stress within the dead zone, a significant amount of mass can accumulate there such that the disc self-gravity starts to affect the structure and evolution of vortices that are produced by the RWI. Results from previous work indicate that self-gravity tends to stabilize vortex forming instabilities. Linear stability analysis (Lovelace & Hohlfed 2013) predicts that self-gravity can inhibit modes with azimuthal wavenumbers $m < (\pi/2)/(hQ)$, where h is the disc aspect ratio and Q the Toomre stability parameter. In presence of self-gravity, suppression of modes with low m values has also been observed both in 2D (Lin & Papaloizou 2011) and 3D (Lin 2012) simulations of vortices forming at the edge of the gap opened by a giant planet. For a disc which initially presents a density bump where the RWI can grow, this has also been reported in the simulations of Zhu & Baruteau (2016), who also found that large-scale vortices are significantly weakened when self-gravity is included. In fact, it is expected that self-gravity can affect vortex dynamics in discs with $Q \lesssim 1/h$ (Regály et al. 2012; Yellin-Bergovoy, Heifetz & Umurhan 2016), which suggests a possible important role of self-gravity on the RWI for moderately massive discs. This has been recently confirmed by Regály & Vorobyov (2017) who have shown that vortices developed at sharp viscosity transitions can be significantly stretched by the effect of self-gravity in low-mass discs with masses $0.001 \leq M_{discs}/M_{\star} \leq 0.01$, where $M_{\star}$ is the mass of the central star. This basically arises because the vortex exerts a negative (resp. positive) torque on the gas material located ahead (resp. behind) of the vortex which, combined with the effect of Keplerian shear, results in the vortex being significantly stretched in the azimuthal direction. As mentioned by Regály & Vorobyov (2017), however, it is not clear whether or not vortex stretching can overcome the effect of self-gravitational contraction in more massive discs.

In this paper, we examine by means of 2D hydrodynamical simulations the effect of self-gravity on the evolution of vortices that are formed at the inner edge of the dead zone in massive discs with $Q_{init} \leq 30$, where Q_{init} is the initial value for the Toomre parameter at the location of the viscosity transition. The aim is to test whether gravitational condensation can eventually stabilize the vortex structure in massive discs, and how this depends on the equation of state that is adopted. The paper is organized as follows. In Section 2 we describe the hydrodynamical model and the initial conditions that are used in the simulations. In Section 3 we discuss the effect of self-gravity on the evolution of vortices in both isothermal discs while we consider the case of non-isothermal discs in Section 4. Finally, we discuss our results and draw our conclusions in Section 5.

2 THE HYDRODYNAMICAL MODEL

2.1 Numerical setup

Simulations were performed using the GENESIS (De Val-Borro et al. 2006) numerical code which solves the equations governing the disc evolution on a polar grid (R, ϕ) using an advection scheme based on the monotonic transport algorithm (Van Leer 1977). It uses the FARGO algorithm (Masset 2000) to avoid time step limitation due to the Keplerian velocity at the inner edge of the disc, and includes a module to calculate self-gravity using a Fast Fourier Transform method (Baruteau & Masset 2008). In order to take into account the effect of the finite disc thickness, the gravitational potential is smoothed out using a softening length $\epsilon_{SG} = bR$ with $b = 0.6h$ (Muller & Kley 2012; Zhu & Baruteau 2016). We emphasize that the indirect term of the gravitational potential has been included in the simulations presented here. Previous work has demonstrated that including this term tends to strenghen large-scale vortices (Zhu & Baruteau 2016; Regály & Vorobyov 2017) so that it is important to include this term when considering the evolution of vortices formed at a viscosity transition.

We adopt computational units such that the mass of the central star $M_* = 1M_{\odot}$, the gravitational constant $G = 1$, and the radius $R = 1$ in the computational domain corresponds to 0.3 au. When discussing the results of the simulations, time will be measured in units of the orbital period at $R = 3.5$ that corresponds to the location of the pressure bump where the RWI is generated.

The simulations presented here employ $N_R = 792$ radial grid cells logarithmically distributed between $R_{in} = 1$ and $R_{out} = 12.5$, and $N\phi = 1280$ grid cells in azimuth.

In this work, we will examine the evolution of vortices in isothermal and radiative disc models. In both cases, the effective kinematic viscosity is modelled using the standard α prescription $\nu = \alpha c_s^2/\Omega$ (Shakura & Sunyaev 1973), where c_s is the isothermal sound speed, Ω the angular velocity, and α is the viscous stress parameter that can vary from very small values in the dead zone to much higher values in the active region.

2.1.1 *Isothermal disc models*

For the isothermal disc models, the α profile that we employ is given by:

$$\alpha = \frac{\alpha_a - \alpha_d}{2}\left[\tanh\left(\frac{R - R_{idz}}{\Delta R_{idz}}\right) - 1\right] + \alpha_a \quad (1)$$

where $\alpha_a = 10^{-2}$ is the α value in the active region, whereas the α viscosity inside the dead zone is set to $\alpha_{dz} = 10^{-4}$. We note that adopting a non-zero value for α_{dz} is in agreement with the results of 3D magnetohydrodynamical simulations (Okuzumi & Hirose 2011; Gressel et al. 2012), which show that the dead zone has a small residual viscosity due to the propagation, inside the dead zone, of sound waves generated in the active region. In the previous equation $R_{idz} = 3.5$ corresponds to the location of the inner edge of the dead zone and ΔR_{idz} is the radial width of the viscosity transition which is set to $\Delta R_{idz} = H_{idz}$, where H_{idz} is the disc scaleheight at $R = R_{idz}$.

2.1.2 *Non-isothermal and radiative disc models*

The energy equation that is implemented in the code for the radiative disc models reads:

$$\frac{\partial e}{\partial t} + \nabla \cdot (e\mathbf{v}) = -(\gamma - 1)e\nabla \cdot \mathbf{v} + Q^+_{visc} - Q^- \quad (2)$$

where e is the thermal energy density, $\mathbf{v}$ the velocity, and γ the adiabatic index which is set to $\gamma = 1.4$. In the previous equation, Q^+_{visc} is the viscous heating term (D'angelo et al. 2003) and Q^- is the gas cooling function for which we adopt two different forms. The

first one corresponds to a standard β parametrization for cooling, with (Les & Lin 2015):

$$Q^- = \frac{1}{\tau_{\rm cool}}\left(e - e_{\rm i}\frac{\Sigma}{\Sigma_{\rm i}}\right) \quad (3)$$

where $e_{\rm i}$ and $\Sigma_{\rm i}$ are the initial thermal energy and surface density which are set in such a way that both the aspect ratio and surface density profiles coincide to those of the isothermal runs just before the random perturbations that will give rise to vortices are applied (see Section 2.2). $\tau_{\rm cool}$ is the cooling time which is set to $\tau_{cool} = \beta\Omega^{-1}$, with β the cooling parameter. In this work, we considered values for β running from $\beta = 0.01$ to $\beta = 1$. We emphasize that in the context of gravitational instabilities, a disc that becomes gravitationally unstable can fragment for these values for β (Gammie 2001). Here, the disc is initially stable regarding the development of gravitational instabilities since $Q_{init} \gtrsim 2$ at all radii and for all models that we consider. Whenever the cooling term given by equation (3) is employed, we also note that an additional source term is also included in the energy equation by changing Q^+_{visc} to $Q^+_{\rm visc} - Q^+_{{\rm visc},i}\frac{\Sigma}{\Sigma_i}$ to ensure that the heating and cooling terms couterbalance initially, where the index i denotes the initial evaluation of the quantities Q, Σ.

We also considered models with more realistic cooling instead of β cooling. In that case the cooling function is similar to that used in Faure et al. (2015) and is given by:

$$Q^- = b\Sigma(T^4 - T^4_{\rm irr}) \quad (4)$$

where $T = \mu(\gamma - 1)e/R\Sigma$ is the temperature, with R the gas constant and $\mu = 2.3$ the mean molecular weight, b is the cooling parameter, and $T_{\rm irr}$ is the irradiation temperature with:

$$T^4_{\rm irr} = 0.1\left(\frac{R_\star}{R}\right)^2 T^4_\star \quad (5)$$

where $T_\star = 4300K$ is the stellar temperature, $R_\star = 2R_\odot$ the stellar radius, and where the factor of 0.1 accounts for the component of stellar irradiation that is normal to the disc equatorial plane (Zhu et al. 2012). A constant value is adopted for the cooling parameter b in equation (4), and is chosen in such a way that the disc aspect ratio h at the inner edge of the disc corresponds to a chosen value $h = h_{in}$. Given that $Q^+_{visc} = \frac{9}{4}\nu\Sigma\Omega^2$ and $Q^- \sim b\Sigma T^4$ in the active region, the condition of thermal equilibrium implies:

$$b = \frac{9R^4\alpha_{\rm a}}{\mu^4 h^6_{in} R^6_{in}\Omega^5_{in}} \quad (6)$$

where Ω_{in} the angular velocity at $R = R_{in}$.

To allow for a direct comparison with the results of Faure et al. (2015), the runs with realistic cooling include a different function for α:

$$\alpha = \begin{cases} \alpha_{\rm a} & \text{if } T \geq T_{\rm MRI} \\ \alpha_{\rm dz} & \text{if } T < T_{\rm MRI} \end{cases} \quad (7)$$

where $T_{\rm MRI} = 1000$ K is the critical temperature above which the MRI is supposed to be at work due to thermal ionization of alkali metals (Umebayashi & Nakano 1988). It is important to note that the results for such runs may not be easily compared to those corresponding to a non-isothermal setup with β cooling. This is because (i) equation (7) employs a feedback loop between the temperature and viscosity which is responsible for the vortex cycles observed in the simulations of Faure et al. (2015) and (ii) compared to the case where α is given by equation (1), equation (7) gives rise to a much sharper viscosity transtion whose width corresponds typically to that of one grid cell, and this is expected to give rise to a stronger vortex with longer lifetime (Regály et al. 2012).

In these runs, we also model the turbulent diffusion of heat by adding in the right-hand side of equation (2), a diffusion term for the gas entropy $S = p/\Sigma^\gamma$, where p is the pressure, and which is given by $D = \kappa e\nabla^2 \log S$. The thermal diffusion coefficient κ is chosen assuming a Prandtl number $P_R = \nu/\kappa$ of unity, which is consistent with the results of Pierens et al. (2012) who found $P_R \sim 1.2$ in non-isothermal disc models with turbulence driven by stochastic forcing. Within the dead zone, we note that radiative diffusion can possibly dominate over turbulent transport for diffusing entropy (Latter & Balbus 2012), so we expect the Prandtl number in a realistic protoplanetary disc model to be close to unity only in the active region.

2.2 Initial conditions

The isothermal disc models that we consider have constant aspect ratio $h = 0.05$ that corresponds to a fixed temperature profile that varies as $T \propto R^{-1}$. A similar initial temperature profile is used in the non-isothermal disc models. In the case where the β cooling prescription is adopted, the cooling function given by equation (4) tries to restore the initial temperature profile, whereas in the case where a more realistic cooling is used, the temperature profile at steady state can differ significantly from the original one. In both cases, however, the aspect ratio at the disc inner edge is kept fixed with a value of $h = h_{in} = 0.05$.

The initial disc surface density is $\Sigma = f\Sigma_{in}(R/R_{in})^{-3/2}$ where f is a scaling factor for which we consider values of $f = 1, 2, 4, 8$ and Σ_{in} is defined such that for $f = 1$, the initial surface density at 1 au in the unperturbed disc is $\sim$870 g/cm^2. This corresponds to a disc mass M_d contained within the computational domain of $M_d \sim 0.002\ M_\star$, whereas $M_d \sim 0.02$ for $f = 8$.

To trigger the RWI within the disc, we proceed in two steps. We first make a pressure bump form and evolve as a result of the radial viscosity transition given by equation (1) or (7), until the amplitude of the density bump is five times the initial surface density. In the upper left and upper right panels of Fig. 1, we plot for the radiative case the resulting surface density and temperature profiles at that time, which corresponds to $t \sim 380$ orbits at the location of the pressure bump. The lower left panel of Fig. 1 shows the Toomre Q parameter,

$$Q = \frac{\Omega c_{\rm s}}{\pi G\Sigma}$$

as a function of radius. As expected, the Toomre parameter is maximal in the active region due to the higher temperature there, and minimal at the location of the pressure bump, with values ranging from $Q \sim 15$ for $f = 1$ down to $Q \sim 2$ for $f = 8$. Finally, the lower right panel of Fig. 1 displays the radial profile of the function:

$$L = \frac{\Sigma}{\omega}\left(\frac{p}{\Sigma^\gamma}\right)^{2/\gamma} \quad (8)$$

where ω is the vertical component of the vorticity. According to linear theory (Lovelace et al. 1999; Li et al. 2000, 2001), we expect the disc to be unstable to the RWI at the location where the function L presents a maximum in its radial profile, namely at the location of the pressure bump from the lower right panel of Fig. 1. This is also valid when an isothermal equation of state is adopted, with the maximum in the L function corresponding to a minimum of the potential vorticity in that case.

The RWI is triggered by adding a $10^{-2}c_{\rm s}$ amplitude white noise to the radial component of the velocity, which subsequently leads

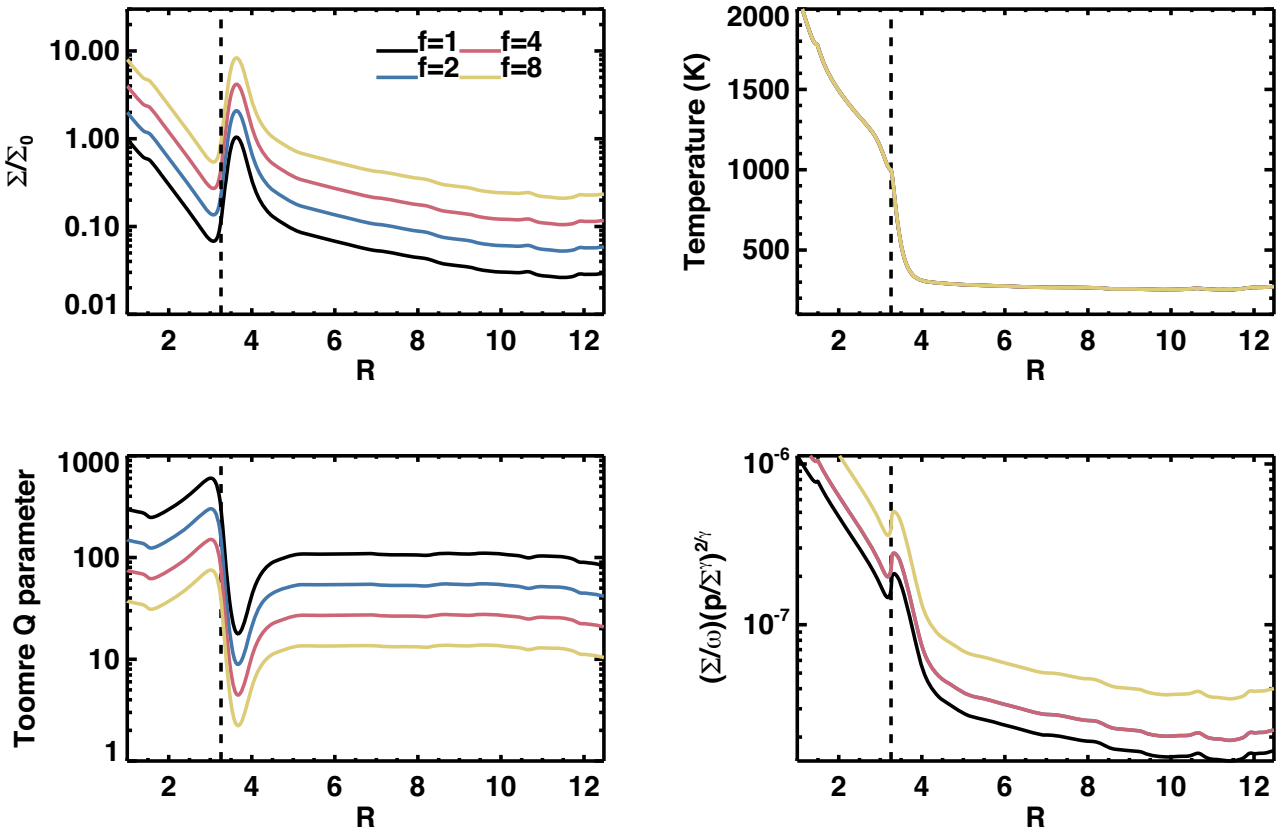

Figure 1. Radial profiles of the surface density (upper left panel), temperature (upper right panel), Toomre parameter (lower left panel), and L function defined as $L = (\Sigma/\omega)(p/\Sigma^{\gamma})^{2/\gamma}$. These profiles correspond to the initial conditions in radiative disc models for $f = 1, 2, 4, 8$. The vertical dashed line shows the location of the viscosity transition.

to the formation of vortices at the surface density maximum after ∼10 orbits.

2.3 Boundary conditions

To avoid wave reflection at the edges of the computational domain, we employ damping boundary conditions (de Val-Borro et al. 2006) using wave killing zones for $R < 1.5$ and $R > 12$ where the surface density, internal energy, and velocity components are relaxed towards their values at the end of the first step (see Section 2.2), namely prior to the addition of the random perturbation. As will be discussed later in the paper, interaction with a massive vortex can make the disc become globally eccentric. In that case, results from previous studies (Papaloizou 2005, Kley & Dirksen 2006) suggest that the boundary conditions we adopt are well suited to hydrodynamical simulations of eccentricity protoplanetary discs. We note that in test simulations employing an outflow boundary condition at the inner edge, significant growth of the disc eccentricity was not observed, due to the overestimated loss of material and radial kinetic energy through the inner boundary, which is in agreement with the results of Papaloizou (2005).

2.4 Diagnostics

To estimate the vortex strength, we calculate the Rossby number Ro which is defined as the dimensionless vertical component of the vorticity relatively to the background flow:

$$Ro = \frac{\mathbf{e_z} \cdot (\nabla \wedge (\mathbf{v} - R\Omega_K \mathbf{e}_\phi))}{2\Omega_K(R_v)} \tag{9}$$

Strength of the vortex can be estimated by measuring Ro at vortex center. Regarding other vortex characteristics, its aspect ratio χ_v can be determined by first locating the vortex boundary that we define as the contour where $\Sigma = 0.5 \max(\Sigma)$. Assuming that the shape of this contour is close to that of an ellipse, we can then estimate the vortex aspect ratio simply as $\chi_v = a/b$, where a and b are the semimajor and semiminor axes of the ellipse, respectively.

Other diagnostic quantities include:

(i) The reynolds stress α_R which is given by:

$$\alpha_R = \frac{2}{3}\frac{\langle \Sigma \delta v_R \delta v_\phi \rangle}{\langle \Sigma c_S^2 \rangle} \tag{10}$$

where denotes an azimuthal average over the entire disc, $\delta v_R = v_R - v_R$, $\delta v_\phi = v_R - v_\phi$

(ii) The gravitational stress α_G which is given by:

$$\alpha_G = \frac{2}{3}\frac{\langle \int_{-\infty}^{\infty} (4\pi G)^{-1} g_R g_\phi \mathrm{d}z \rangle}{\langle \Sigma c_s^2 \rangle} \tag{11}$$

where g_R ang g_ϕ are the radial and azimuthal components of the self-gravitational acceleration. The vertical integration is performed by changing the square of the smoothing parameter b^2 to $b^2 + \eta^2$ where η is such that $z = \eta R$ (Baruteau, Meru & Paardekooper 2011). Following Bae et al. (2014), η is varied evenly by 0.01 from zero to one.

3 EVOLUTION IN ISOTHERMAL DISCS

We begin our description of the evolution of vortices in self-gravitating discs by examining the results of the isothermal simulations. In the isothermal limit, we note that because the pressure bump acts as a trap for the vortex, vortex migration is not expected in that case (Paardekooper et al. 2010).

In these runs, the growth timescale of the RWI is typically $t_{growth} \sim 5$ orbits, this value is found to be nearly independent of whether self-gravity is taken into account or not. The most unstable azimuthal wavenumber m_{max} of the RWI, however, is found to be slightly higher in the case where self-gravity is included. For the model with $f = 1$, for example, $m_{max} = 6$ in the simulation without self-gravity, where $m_{max} = 7$ if self-gravity is included. This is exemplified in the first panel of Fig. 2 which shows, for this model, a snapshot of the disc surface density at $t = 5$ orbits.

The non-linear evolution of the RWI in simulations with self-gravity, however, significantly differs from that in runs where self-gravity is not considered. In the case where self-gravity is discarded, a long-lived vortex with aspect ratio $\chi \sim 4$–5 develops, whereas when self-gravity is included, two different modes of evolution are obtained, depending on the disc mass. For models with $f = 1$, 2, a single vortex that is formed ultimately decays due to the mechanism described in Regály & Vorobyov (2017), whereas for $f \geq 4$, a vortex with a turbulent core undergoes gravitational contraction. We now describe in more details these two modes of evolution.

We use the run with $f = 1$ to illustrate the first mode of evolution that we find. For this calculation, contours plots of the surface density at four representative times are displayed in Fig. 2. The second panel corresponding to $t = 500$ reveals that at that time, the initial vortices have merged to form a single vortex with $\chi \sim 5$. At $t = 1000$, however, we see that the vortex aspect ratio has considerably increased while the azimutal surface density contrast has decreased. The surface density structure at $t = 1500$ (fourth panel) suggests that the vortex stretches out until it completely dissipates in the background flow. This process is further illustrated in Fig. 3 where we show the time evolution of the Toomre parameter at vortex center Q_v (upper panel), vortex aspect ratio χ_v (middle panel), and Rossby number of the vortex Ro (Lower panel). The continuous decrease in $|Ro|$ in the time period between 600 and 1200 orbits confirms that the vortex weakens as vortex stretching occurs. At $t \sim 1200$, $Ro \sim 0$ which indeed indicates that the vortex has been almost entirely suppressed at that time. A new elongated vortex whose evolution is very similar to that described above eventually emerge at later times, thereby giving rise to cycles of vortex formation-dissipation. One such cycle is illustrated by the sequence of snapshots at four successive times that is presented in Fig. 6. We note that similar vortex mode oscillations have also been reported in previous non self-gravitating simulations of vortices forming at a viscosity transition (Regály et al. 2012).

The mechanism of vortex decay that is observed in the simulations may arise for two reasons.

First, the vortex excites spiral density waves that can turn into shocks once the vortex amplitude becomes high enough. This not only causes the vortex to lose energy through shock dissipation, but also can significantly alter the background vortensity (i.e. the ratio between the vertical component of the vorticity and the disc surface density) profile. The gap-opening criterion of Crida et al. (2006) predicts that the vortex should be able to carve a gap in the disc provided that $P < 1$, where P is the gap opening parameter which is given by:

$$P = 1.1 \left(\frac{q_v}{h^3}\right)^{-1/3} + \frac{50\nu}{q_v R_v \Omega_v} \tag{12}$$

where R_v is the radial position of the vortex, q_v is the vortex-to-star mass ratio, and Ω_v the angular velocity at this location. For the runs with $f = 1$ and $f = 2$, we estimate that at the time where the vortex begins to decay $q_v \sim 1.3 \times 10^{-4}$ and $q_v \sim 2.8 \times 10^{-4}$, respectively. This gives $P \sim 0.85$ for the run with $f = 2$, whereas $P \sim 1.1$ in the case with $f = 1$. Therefore, we expect the background vortensity profile to be only weakly altered in the simulation with $f = 1$, while the background vortensity gradient might be significantly smoothed out by the vortex in the run with $f = 2$. Compared to the case of a gap carved by a planet, however, we note that for a vortex the aforementioned gap-opening criterion may also depend strongly on the vortex aspect ratio, since we expect elongated vortices to be much less efficient in modifying the background vortensity profile than nearly circular ones. For the simulations including self-gravity, we show in the upper panel of Fig. 4 the vortensity profile at the time where the vortex begins to decay, and which can be different for distinct models. For the non self-gravitating case, the vortensity profiles at the same times are also plotted for comparison in the lower panel of Fig. 4. Contrary to our own expectation, the non self-gravitating vortex seems to be more efficient in changing the background vortensity profile than the self-gravitating one. This is confirmed by inspecting the time evolution of the Reynolds stresses, which is presented in Fig. 5. We see that the stresses are slightly higher in the non self-gravitating case, which demonstrates that the spiral waves induced by the non self-gravitating vortex are more efficient in changing the background vortensity profile. This is consistent with the non self-gravitating vortex having a smaller aspect ratio, thereby exciting stronger spiral wakes. Despite its ability to modify the background, the non self-gravitating vortex appears to remain fairly stable over the course of the simulation, such that we can conclude that the mechanism of vortex decay that is observed in the self-gravitating simulations is not related to spiral shocks induced by the vortex.

Secondly, vortex decay can occur due to the self-gravitational torque of the vortex, as described in Regály & Vorobyov (2017). These authors showed that the contribution of the self-gravitational torque acting on the leading part of the vortex is negative, whereas the trailing part of the vortex undergoes a positive torque. This, combined with the effect of Keplerian shear, leads to the vortex being continuously stretched out until it completely dissipates in the background flow. Such a mechanism is estimated to be responsible for vortex decay in discs with masses $M_{disc}/M_\star \gtrsim 0.005$ (Regály & Vorobyov 2017), which is equivalent to $Q \lesssim 50$ at the location of the viscosity transition in the unperturbed disc phase. Here, our runs with $f = 1$, 2 in which vortex stretching arises have $Q \sim 30$ and $Q \sim 15$ in the unperturbed disc, respectively, which is consistent with the estimation of Regály & Vorobyov (2017).

Simulations with $Q \leq 7$ and which correspond to models with $f = 4$, 8 resulted in a different outcome. As mentionned earlier, the vortex undergoes gravitational collapse in that case. To illustrate how evolution proceeds in that case, we use the run with $f = 4$ and for which the vortex structure in terms of surface density and Rossby number at different times is presented in Fig. 7. Similar to the run with $f = 1$, merging of initial vortices gives rise to a single vortex whose structure is strongly affected by self-gravity. At $t = 650$, one can see that the vortex is indeed significantly elongated due to a mechanism presented in Regály & Vorobyov (2017), with an aspect

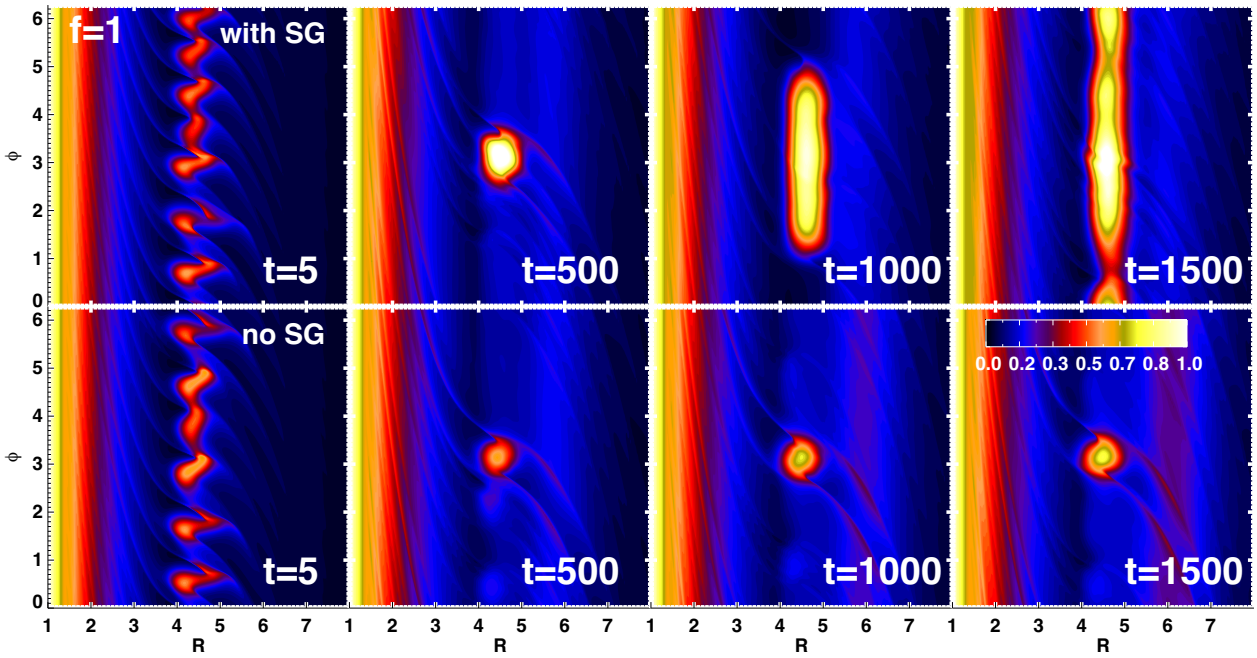

Figure 2. *Upper panel:* contours of the scaled surface density Σ/Σ_{in} at different times for the isothermal run with $f = 1$ and with self-gravity included. *Lower panel:* same but in the case where self-gravity is not included.

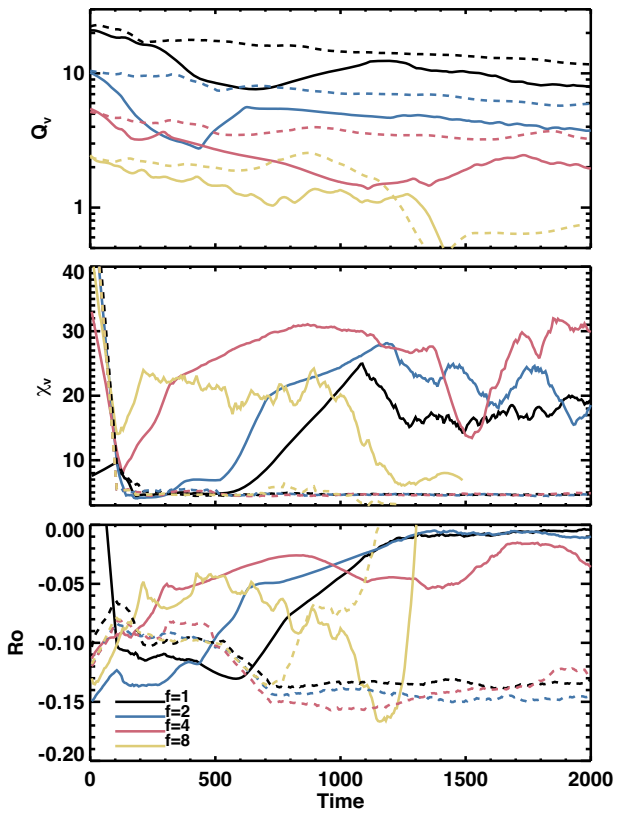

Figure 3. *Upper panel:* Evolution of the Toomre parameter at vortex centre, averaged over 100 orbital periods at vortex location, for the isothermal runs with, from top to bottom, $f = 1$, 2, 4, 8. The solid lines correspond to simulations including self-gravity, whereas the dashed lines correspond to non self-gravitating runs. *Middle panel:* same but for the vortex aspect ratio χ_v. *Lower panel:* same but for the Rossby number calculated at vortex centre.

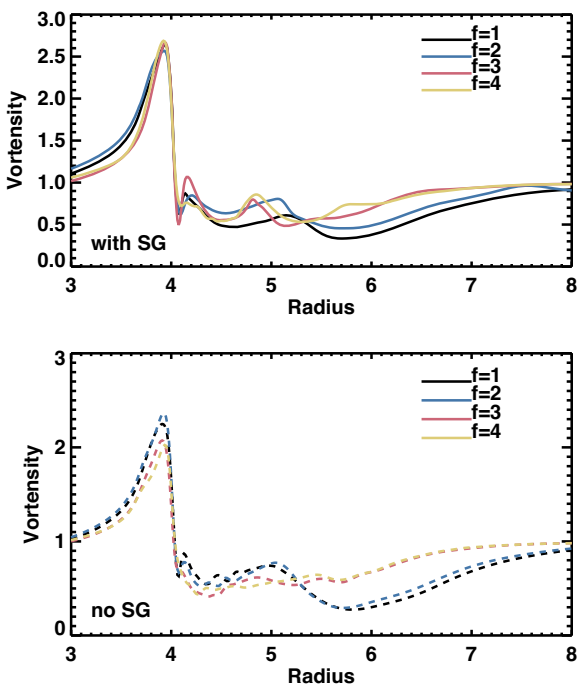

Figure 4. *Upper panel:* Radial profile of the disc vortensity prior vortex decay occuring, for the isothermal simulations that include self-gravity. *Lower panel:* Vortensity profile at the same times but for runs that do not include the effect of self-gravity.

ratio estimated to $\chi \sim 18$. Contrary to models with $Q \geq 15$, however, the ellipsoidal vortex does not dissipate but rather strenghens at later times, which is confirmed by inspecting in Fig. 3 the evolution of *Ro* that is continuously decreasing for $900 < t < 1100$. This decrease in *Ro* is accompanied by a decrease in χ, thereby sug-

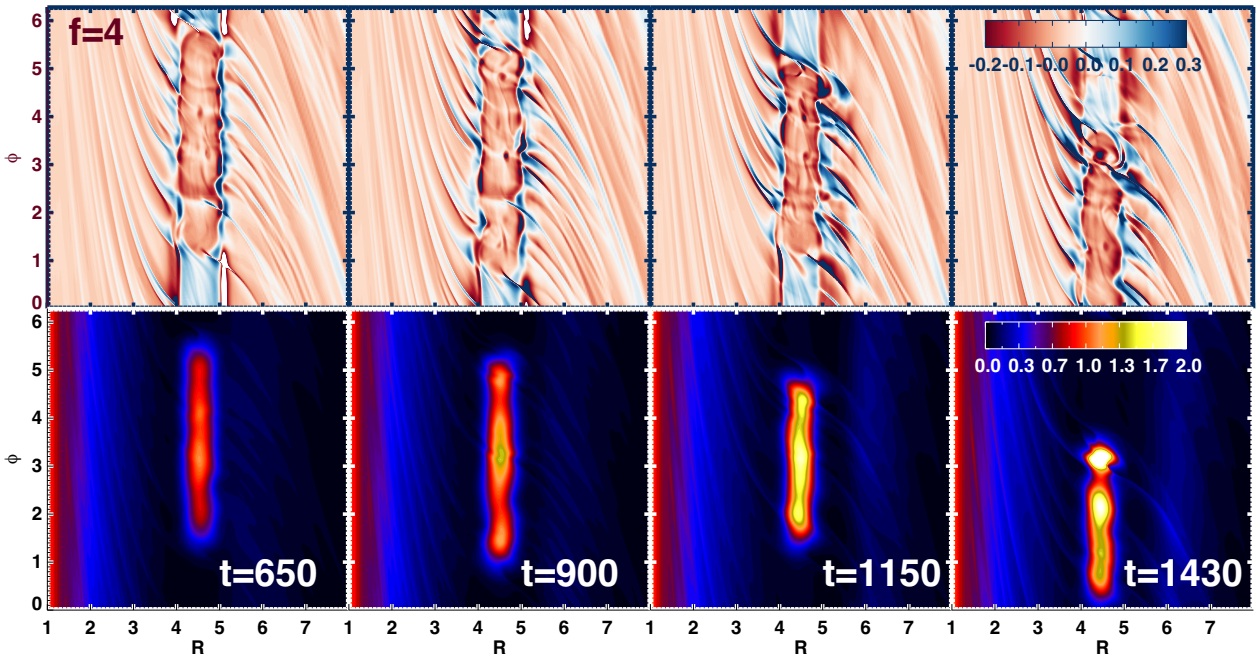

Figure 5. *Upper panel:* Time evolution of the Reynolds α_R and gravitational stresses α_G for the isothermal simulations that include self-gravity. The horizontal dashed line corresponds to the value for the viscous stress parameter employed in the dead zone. *Lower panel:* Time evolution of the Reynolds stress α_R for the runs without self-gravity.

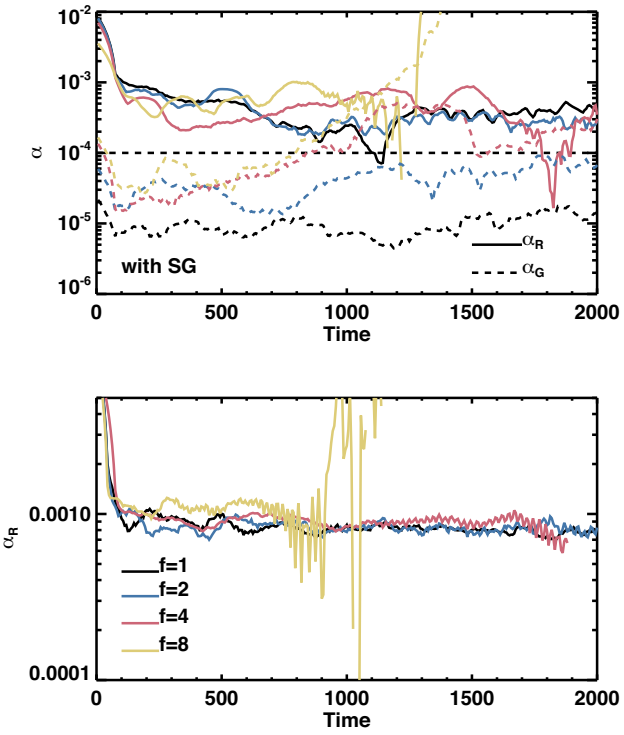

Figure 6. Contours of the scaled surface density Σ/Σ_{in} at different times for the isothermal, self-gravitating run with $f = 1$ and illustrating the cycles of vortex formation–dissipation that are obtained at the end of the simulation.

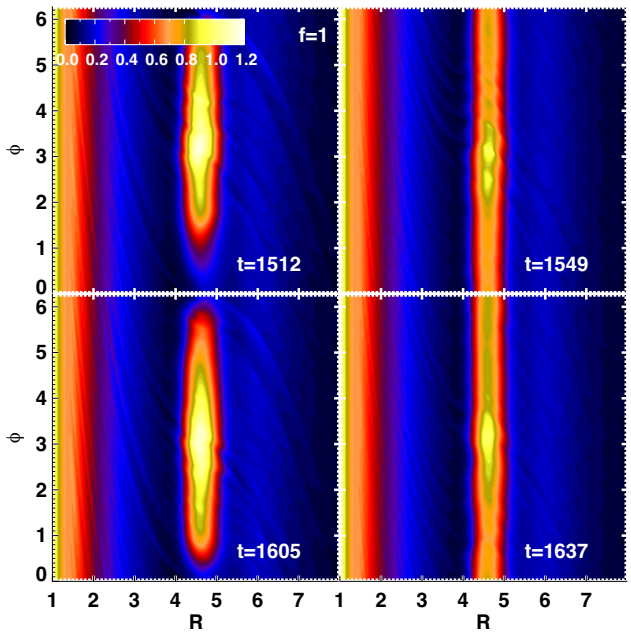

Figure 7. *Upper panel:* contours of the Rossby number at different times for the isothermal run with $f = 4$ and with self-gravity included. *Lower panel:* contours of the scaled surface density $\Sigma/(f\Sigma_{in})$ at different times for the same run.

gesting self-gravitational contraction of the vortex. As the vortex contracts, the surface density at vortex centre increases, which is unambiguously supported by looking at the vortex surface density maps at $t = 900$ and $t = 1150$ in Fig. 7. Inspection of contours of the Rossby number at $t = 1150$ also shows that gravitational instabilities can develop within the vortex core. For simulations including self-gravity, gravitational stresses α_G together with Reynolds stresses α_R are plotted as a function of time in the upper panel of Fig. 5. We see that the gravitational stresses continuously increase up to $\alpha_G \sim \alpha_R$, which unambiguously confirms that the vortex core is subject to

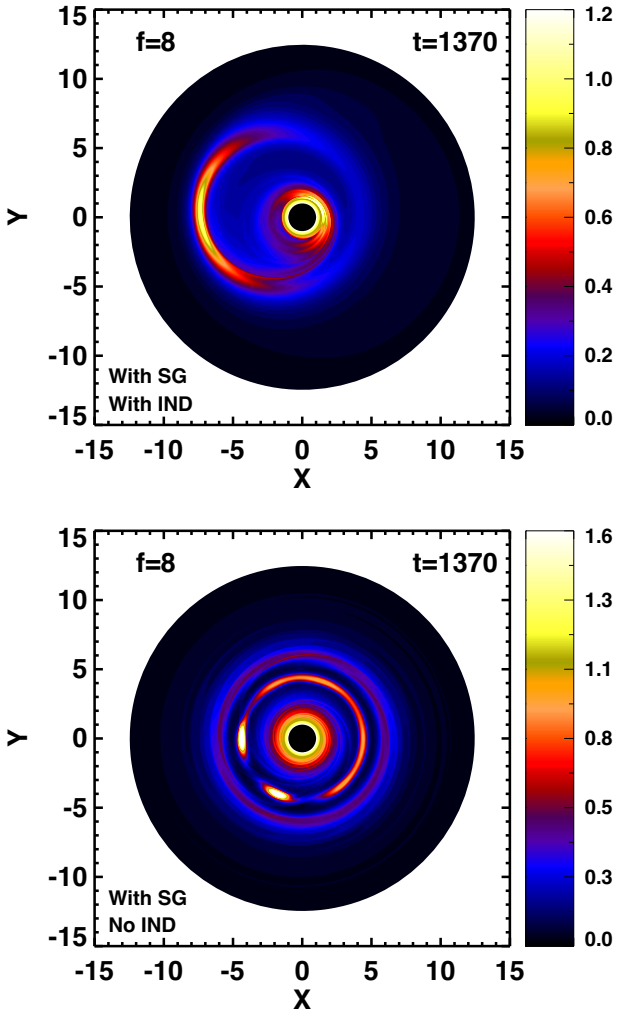

Figure 8. *Upper panel:* snapshot of the disc surface density at $t = 1370$ for the isothermal run with $f = 8$ and including self-gravity and the indirect term of the gravitational potential. *Lower panel:* same but in the case where the indirect term is discarded.

gravitational instabilities. In appendix we show that this result is robust regarding both the numerical resolution that is adopted and the amplitude of the density bump at the end of the first step (see Section 2.2)

As the vortex grows, spiral waves launched by the vortex become stronger and stronger. In Fig. 7, one can clearly see these strong wakes extending from either side of the vortex in the surface density map corresponding to $t = 1430$. These spiral waves contribute to the further gravitational collapse of the vortex by allowing gas accretion onto it. Such a process occurs until a point in time where the vortex becomes strong enough for the spiral waves to turn into shocks, which makes the vortex lose energy and decay through shock dissipation (Les & Lin 2015). The released mass from the vortex subsequently enables the RWI to be relaunched at the location of the pressure bump, which gives rise to the formation of a new vortex whose evolution follows a similar cycle.

In disc models with $f = 8$, we find that the vortex is massive enough to make the disc become globally eccentric, as revealed by looking at contours of the surface density which are plotted at $t = 1370$ in the upper panel of Fig. 8. One possibility to estimate the eccentricity growth within the disc is to compute radial kinetic

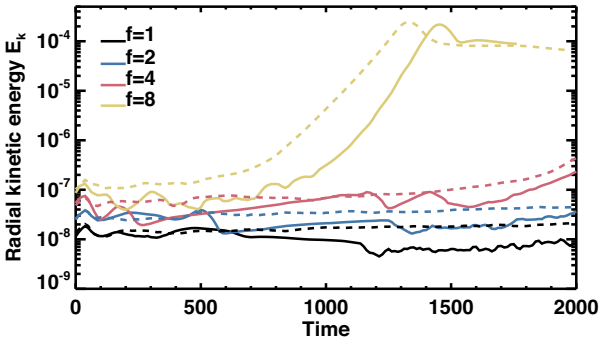

Figure 9. Evolution of the total radial kinetic energy, for the isothermal runs with, from bottom to top, $f = 1$, 2, 4, 8. The solid lines correspond to simulations including self-gravity, whereas the dashed lines correspond to non self-gravitating runs.

energy (Kley & Dirksen 2006, Teyssandier & Ogilvie):

$$E_{\rm k} = \frac{1}{2}\int_0^{2\pi} \Sigma v_R^2 R dR d\theta, \tag{13}$$

whose time evolution is plotted for each run in Fig. 9. Rapid growth of $E_{\rm k}$ is observed for $f = 8$, and this does not depend whether or not self-gravity is included. This implies that self-gravity is not the main engine for driving the instability. Instead, it appears that the growth of the disc eccentricity arises from the effect of the indirect term of the gravitational potential. When the vortex is massive enough, we indeed expect the barycentre of the system to be significantly shifted away from the star, which can cause the development of $m = 1$ gravitational instabilities (Adams, Ruden & Shu 1989). The typical growth rate timescale of such instabilities is expected to not exceed the orbital period as long as $Q \lesssim 3$, which is indeed the case in our runs with $f = 8$. Moreover, neither growth of the kinetic energy nor growth of the disc eccentricity occured in simulations that were carried out without the indirect term included, as can be observed in the lower panel of Fig. 8 which shows contours of the disc surface density at $t = 1370$ for the run with $f = 8$ but in the case where the indirect term for the gravitational potential is discarded. This clearly demonstrates that the indirect term plays a dominant role in triggering the development of the eccentric instability.

4 EVOLUTION IN NON-ISOTHERMAL DISCS

4.1 Models with β cooling

In the context of classical gravitational instabilities, it is now widely accepted that the outcome of such instabilities strongly depends on the thermodynamical state of the disc. Assuming a β cooling prescription for the cooling timescale $\tau_{\rm cool} = \beta\Omega^{-1}$, the disc tends indeed to achieve a self-regulated state with constant Q value for $\beta \gtrsim 10$, whereas lower values for β give rise to disc fragmentation. Results from the previous section naturally lead to the question of how self-gravitating vortices evolve in discs where the isothermal assumption is relaxed. In order to investigate whether or not the evolution of such vortices can be interpreted in the same way as classical gravitational instabilities, we have performed for the case with $f = 4$ additional non-isothermal simulations with β cooling. Simulations that employ a more realistic prescription for cooling will be presented in the next section. Fig. 10 displays, from top to bottom, the time evolution of the Toomre parameter at vortex centre Q_v, vortex aspect ratio χ_v, Rossby Ro number for $\beta = 0.01$, 0.1,

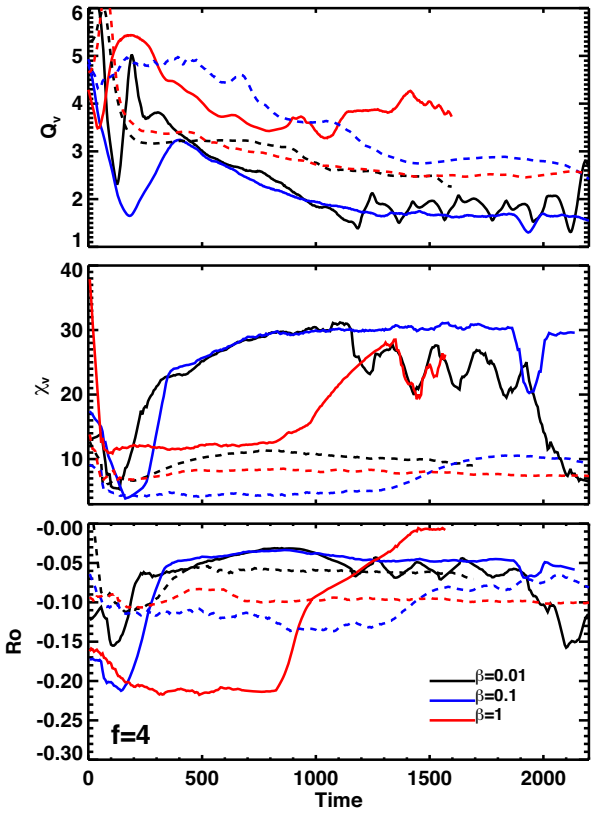

Figure 10. *Upper panel:* Evolution of the Toomre parameter at vortex centre, averaged over 100 orbital periods at vortex location, for the run with $f = 4$ and employing the β cooling prescription. The solid lines correspond to simulations including self-gravity, whereas the dashed lines correspond to non self-gravitating runs. *Middle panel:* same but for the vortex aspect ratio χ_v. *Lower panel:* same but for the Rossby number calculated at vortex centre.

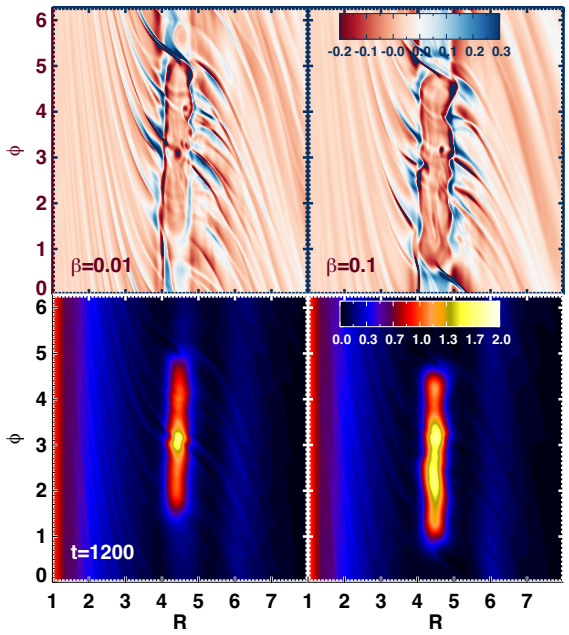

Figure 11. *Upper panel:* contours of the Rossby number at $t = 1200$ and for the runs employing the β cooling prescription with $\beta = 0.01, 0.1$. *Lower panel:* contours of the scaled surface density $\Sigma/(f\Sigma_{in})$.

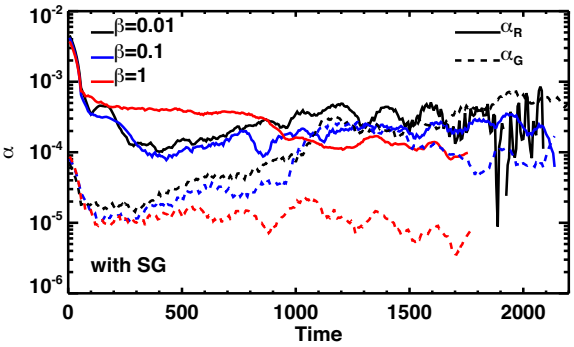

Figure 12. Time evolution of the Reynolds α_R and gravitational stresses α_G for runs with β cooling and that include self-gravity.

1. In non self-gravitating discs, we can see that there is a tendency for the strength of the vortex to increase with β, which is consistent with the results of Les & Lin (2015) who find that the vortex lifetime increases with the cooling timescale.

In self-gravitating discs, the continuous increase in χ_v and subsequent vortex dissipation that is observed in the run with $\beta = 1$ suggest that the self-gravitating torque is at work in that case. We note in passing that models with $f = 1$ (not shown here) also resulted in a similar outcome for $0.01 \leq \beta \leq 1$. In the case where $\beta \leq 0.1$, the results are consistent with the isothermal simulations, with the vortex ultimately collapsing due to the effect of self-gravity. Contrary to the isothermal case, however, we can see that the Toomre parameter at vortex centre reaches an almost constant value $Q_v \sim 1.5$ prior to the vortex collapsing at $t \sim 2000$ orbits (see upper panel of Fig. 10), which is very similar to the value corresponding to a disc reaching a steady gravito-turbulent state. Inspection of Fig. 11 that shows contours of the Rossby number and surface density at $t = 1200$ for both models reveals that gravito-turbulence can indeed develop within the vortex core for $\beta \leq 0.1$. The corresponding alpha parameters α_R and α_G asssociated with the Reynolds and gravitational stresses are shown as a function of time in Fig. 12. During this gravito-turbulent stage, we see that $\alpha_R \sim \alpha_G$, which is consistent with previous studies of gravito-turbulent discs (Gammie 2001; Baruteau et al. 2011). The gravito-turbulence operating in the vortex core may be possibly responsible for the vortex collapse observed at later times through the development of secular gravitational instabilities. This occurs because the anomalous viscosity generated by the hydrodynamic turbulence tends to remove rotational support (Lin & Kratter 2016). For a 2D, self-gravitating, isothermal disc, the dispersion relation for axisymmetric modes with wavenumbers k is given by (Gammie 1996):

$$s = \frac{\nu k^2 (2\pi G|k| - c_s^2 k^2)}{\Omega^2 + c_s^2 k^2 - 2\pi G \Sigma |k|} \tag{14}$$

For $Q \sim 1.5$ and $h = 0.05$, s is positive for perturbations whose scalelength $L = 2\pi/k$ are such that $L \gtrsim H$. The corresponding maximum growth rate s_{max} is given by (Lin & Kratter 2016):

$$s_{max} = \frac{27\alpha}{16Q^4}\Omega \tag{15}$$

For $\alpha = \alpha_R + \alpha_G \sim 10^{-3}$, $s_{max} \sim 3 \times 10^{-4}\Omega$ that corresponds to a growth time of ∼500 orbits. This is very similar to the characteristic time for vortex collapse inferred from the simulations. However, we caution the reader that the estimation given by equation (15) results

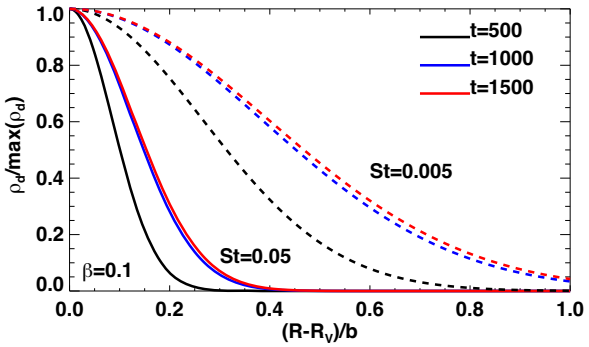

Figure 13. Dust density distribution resulting from the model of Lyra & Lin (2013) and for vortex parameters corresponding to the self-gravitating run with $f = 4$ and using the β cooling prescription with $\beta = 0.1$.

from a linear analysis of secular instabilities that is valid for viscous, Keplerian self-gravitating discs such that it is not clear whether or not it applies to embedded vortices. Moreover, the averaging procedure may also have some impact on the values obtained for α_R and α_G. In fact, we tested the effect of employing an averaging procedure over the vortex surface only and found that stresses are a factor ∼1.3 higher compared to the case where the average is performed over the entire disc. Nevertheless, we can conclude from the above that the slow collapse that is observed is characteristic of secular gravitational instabilities.

4.2 Consequences on dust trapping

The gravito-turbulence arising in the vortex may also have a major impact on dust trapping. To examine this issue in more details, we employ the model described in Lyra & Lin (2013), assuming a GNG model for the vortex. It has been recently shown that vortices developing at sharp viscosity transitions in self-gravitating discs can be well described by such a model (Regály & Vorobyov 2017). According to the model of Lyra & Lin (2013), the dust distribution within the vortex core is given by:

$$\rho_d(x) = \rho_{d,max} \exp\left(-\frac{x^2 b_v^2}{2H_v^2}\right) \quad (16)$$

where we set $x = (R - R_v)/b_v$ with b_v the vortex semiminor axis. H_v is the dusty vortex scaleheight which is given by:

$$H_v = \frac{H}{f(\chi)}\sqrt{\frac{\delta}{St + \delta}} \quad (17)$$

where St is the Stokes number, $f(\chi)$ is a scale function [see equation (35) in Lyra & Lin 2013] and δ is the dimensionless turbulent diffusion coefficient for which we assume $\delta = \alpha_R + \alpha_G$. Focusing on the model with $\beta = 0.1$, we plot for St = 0.005, 0.05 the expected dust distribution at three consecutive times in Fig. 13. Dust grains are initially concentrated close to the vortex centre but as the vortex core becomes gravito-turbulent, increase in the Reynolds and gravitational stresses causes the dust to diffuse away from the vortex centre. We can see that small dust grains with $St = 0.005$ can even be expelled from the vortex due to turbulent diffusion. Assuming a particle density of $\rho_d = 0.8\text{g} \cdot \text{cm}^{-3}$, this would correspond to dust particles with typical radius $a_d \sim 1.5$ cm.

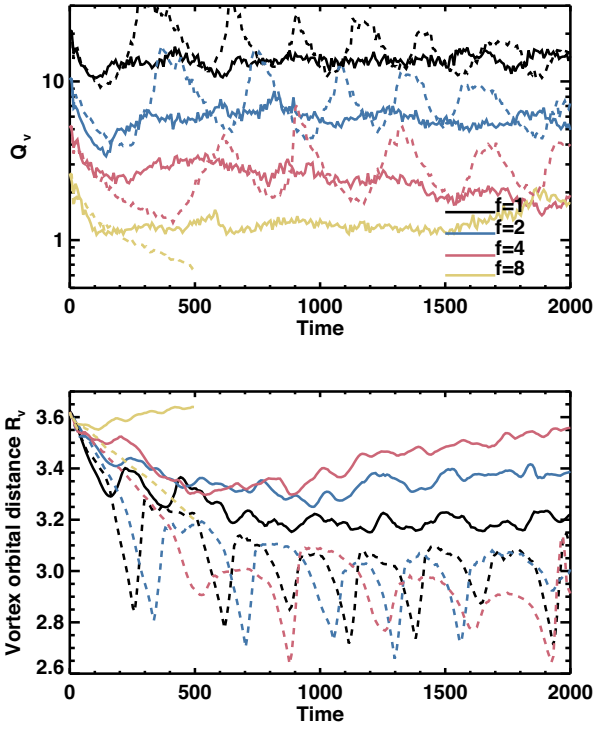

Figure 14. *Upper panel:* evolution of the Toomre parameter at vortex centre, for the radiative runs with, from top to bottom, $f = 1, 2, 4, 8$. The solid lines correspond to simulations including self-gravity, whereas the dashed lines correspond to non self-gravitating runs. *Lower panel:* time evolution of the vortex radial position for the same runs.

4.3 Radiative disc models

We now consider how the evolution of vortices proceeds in a radiative disc, employing a more realistic treatment for the cooling term. For a viscosity function that depends explicitly on temperature [see equation (7)] and gas cooling function given by equation (4), Faure et al. (2015) have reported cycles of formation, migration, and disruption of vortices forming at a pressure maximum. Provided that the vortex does not significantly alter the background vorticity profile, migration of vortices is a priori not expected in that case (Paardekooper et al. 2010). Faure et al. (2015) suggest that vortex migration is associated with a baroclinic term in the vorticity equation, possibly arising from a strong azimuthal temperature gradient. As the cold vortex migrates and penetrates within the much warmer active region, it becomes progressively eroded through diffusion effects, until the released mass gives rise to a new vortex which follows the same evolution.

For our non-isothermal models with $f = 1, .., 8$, the upper panel of Fig. 14 shows the Toomre parameter at vortex centre as a function of time. Similar to the isothermal case, the run with $f = 8$ and in which self-gravity is not included resulted in the growth of the disc eccentricity due to the development of a strong $m = 1$ gravitational instability, whereas for the other non self-gravitating models with $f \leq 4$, Q_v exhibits an oscillating behaviour due to the aforementionned vortex cycles. In the case where self-gravity is included, however, Q_v rather reaches a constant value which suggests that self-gravity can stabilize the vortex against baroclinic effects. Here, the cooling timescale is estimated to be $\tau_{cool} \sim 1/bT^3 \sim 1/\alpha\Omega \sim 16T_{orb}$ which would correspond to $\beta \sim 100$ using the standard β parametrization. The results of these radiative runs therefore suggest that the vortex's

fate is strongly influenced by the details of thermodynamics, since a non-isothermal model with β cooling would give rise to vortex decay for $\beta = 100$. We show in Fig. 15 contour plots of the normalized surface density (upper row) and temperature perturbation relative to the azimuthally-averaged temperature (lower row) for various runs namely: (i) for the case with $f = 1$ and without self-gravity included, prior inward migration of the vortex proceeding and (ii) for the self-gravitating discs with $f = 2, 4, 8$, once the vortex has reached a quasi-equilibrium structure. Comparing the density maps for the two self-gravitating models with $f = 4$ and $f = 8$, it is clear that the vortex becomes denser in more massive discs. As the disc mass increases, however, the temperature inside the vortex also increases, as revealed by inspecting the temperature contours for the two models, which consequently leads to the vortex reaching a constant Q_v value.

The lower panel of Fig. 14 shows for each model the radial position of the vortex R_v as a function of time. It is immediately evident that the vortex cycles are suppressed when self-gravity is taken into account. Consistently with previous simulations of self-gravitating vortices (Zhu & Baruteau 2016), the vortex is observed to even migrate outward in self-gravitating runs with $f \geq 4$. From the maps of the relative temperature perturbation in Fig. 15, we can envision two possible mechanisms that are responsible for the vortex outward migration. First, one can see that the vortex's inner wave tends to be eroded in runs with $f \leq 2$, mainly at the location which corresponds to the transition $T \sim T_{\rm MRI}$. In models with $f \geq 4$, however, the inner wave is much less sheared out, probably because the vortex core is warmer in that case. We note that the inward migration of the non self-gravitating vortex may be partly due to this process, since it tends to increase the asymmetry between the inner and outer waves of the vortex.

Changes in the structure of the outer wake with disc mass can also be identified from these temperature maps, but become more apparent when looking at the Fourier components of the surface density. For the various runs with self-gravity included, the $m = 10$ component of the surface density Σ_m is plotted as a function of $x = (R - R_v)/R_v$ in Fig. 16. We choose such a value for m because in the context of planetary migration, the outer Lindblad torque peaks approximately at $m \sim 10$ for a disc with $h = 0.05$ (Ward 1997). As the disc mass increases, there is a clear trend for the disc response in the outer disc to decrease and for the vortex to become more asymmetric. This tends to reinforce the effect of the vortex's inner wave, and to favor consequently the outward migration of the vortex.

5 DISCUSSION AND CONCLUSION

In this paper, we have presented the results of 2D hydrodynamical simulations that examine the role of self-gravity on the long-term evolution of vortices. These vortices form through the development of the RWI at a pressure bump, which is assumed to be located at the inner edge of a dead zone, where there is a sharp transition in the viscosity parameter α. We focused on the case of massive protoplanetary discs where the Toomre parameter at the location of the pressure bump is initially $Q \leq 30$, and considered both isothermal and non-isothermal equations of state.

For isothermal discs, we find three different modes of evolution depending on the initial value for Q.

i) For $Q \geq 15$, self-gravity makes a large-scale vortex decay due to the self-gravitational torque of the vortex, as predicted by Regály & Vorobyov (2017). Once the vortex has completely dissipated in the background flow, a new vortex emerges at the location of the pressure bump, which follows the same evolution, giving rise to cycles of vortex formation-dissipation.

ii) Isothermal models with $3 \lesssim Q \lesssim 7$ result in the formation of an elongated vortex with aspect ratio $\chi \sim 20-30$ and whose core is found to be turbulent due to the development of gravitational instabilities. At later times, however, the vortex strengthens due to gravitational collapse but is ulimately found to decay once the spiral waves launched by the vortex become too strong. Eventually, a new vortex can emerge at the location of the pressure bump and which follows a similar evolution.

iii) More massive discs with $Q \lesssim 3$ become globally eccentric due to the growth of a $m = 1$ mode in the disc. In that case, it appears that destabilization of the system is not caused by the effect of self-gravity but rather occurs because the vortex is massive enough to significantly shift the barycentre of the system away from the central star.

Vortex decay is also observed in β cooling discs with $\beta \geq 1$ due to the combined effect of self-gravity and Keplerian shear. In models with $\beta \leq 0.1$, gravito-turbulence can operate in the vortex core in models with $3 \lesssim Q \lesssim 7$, with the core maintaining a constant Q_v value. Similar to the isothermal case, the vortex collapses at later times, possibly because anomalous viscosity arising from gravito-turbulence within the disc tends to remove rotational support.

Regarding radiative disc models where the viscosity depends on a switch to disc temperature, non self-gravitating simulations resulted in cycles of vortex formation-migration-disruption, in good agreement with previous work (Faure et al. 2015). Including self-gravity however, causes the vortex cycles to be completely suppressed. This was found to occur because the vortex tends to be warmer and more asymmetric in self-gravitating discs. In that case, a quasi-steady state is reached for which the vortex lasts for $O(10^3)$ orbits and has aspect ratio of $\chi_v \sim 3$–4.

Our results suggest that self-gravity makes difficult forming long-lived vortices at a pressure bump, both in isothermal disc and non-isothermal discs that employ the β cooling prescription. In a radiative disc model where is implemented a better treatment of thermodynamics, however, self-gravity can give rise to a stable vortex structure with aspect ratio $\chi_v \sim 3$–4. Strong vortices with aspect ratio $\chi < 4$ are known to be destroyed by the elliptical instability (Lesur & Papaloizou 2009; Richard et al. 2013). Moreover, we note that in this work vortices are formed on a timescale corresponding to ∼10 orbits, which is comparable to the elliptical instability growth timescale in 3D discs. Therefore, it is not clear whether or not a vortex formed at a pressure bump might be able to survive the elliptical instability, and 3D simulations are clearly required to investigate this issue in more details. 3D simulations including self-gravity and that examine the possible role of the elliptical instability on the evolution of vortices, together with the effect of self-gravity on the elliptical instability will be presented in a future study (Lin & Pierens 2018).

APPENDIX: NUMERICAL ISSUES

To assess the impact of numerics on the results presented in this paper, we performed a suite of additional simulations for various resolutions and different amplitudes for the initial density bump. The upper panel of Fig. 17 shows, for the self-gravitating model with $f = 4$, the time evolution of the Toomre parameter at vortex centre Q_v for runs with our nominal resolution (792 × 1280), increased grid resolution (1584x2560), and lower grid resolution (396 × 640). These three simulations exhibit different relaxation

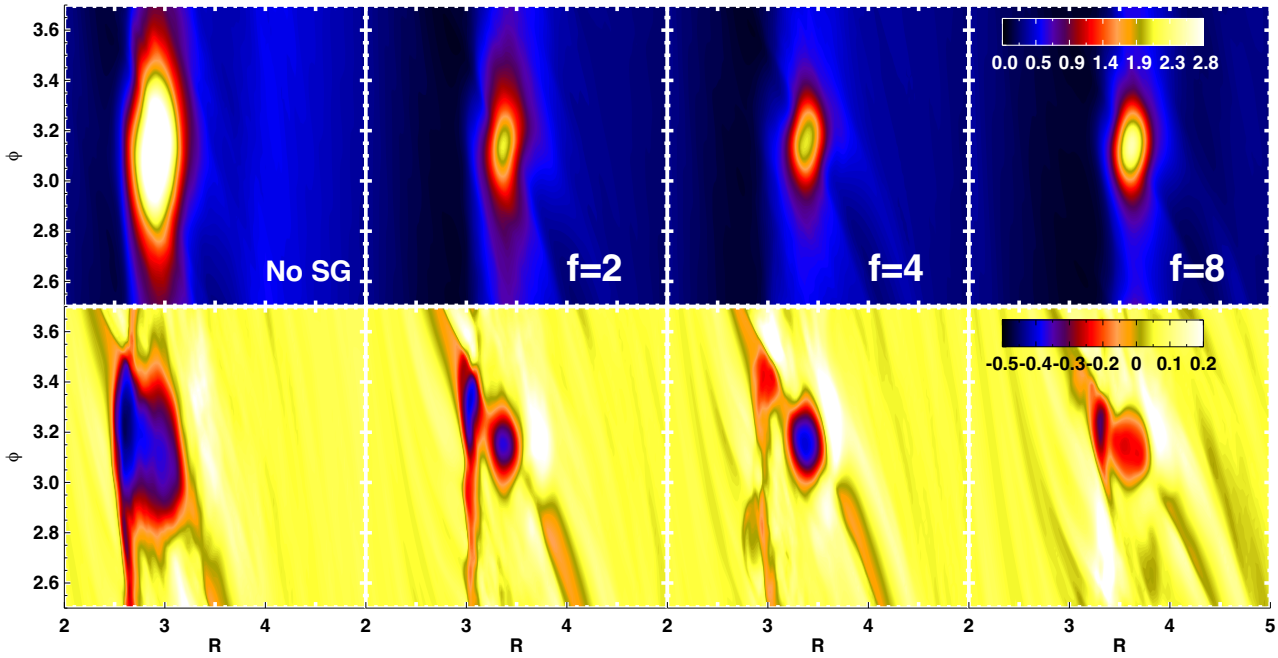

Figure 15. *Upper panel:* contours of the scaled surface density $\Sigma/(f\Sigma_{in})$ at quasi-steady state for the radiative runs. *Lower panel:* Map of the temperature perturbation (relative to the azimuthally-averaged temperature) for the same runs.

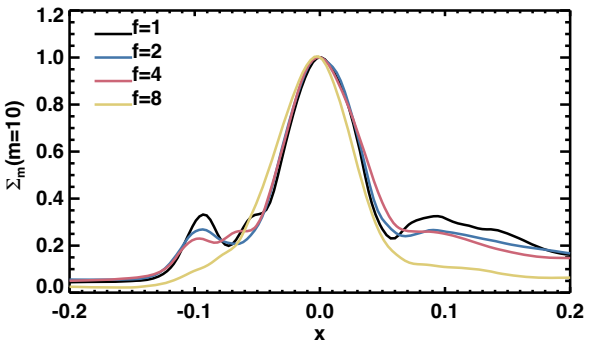

Figure 16. $m = 10$ Fourier component of the surface density as a function of $x = (R - R_v)/R_v$ for the radiative runs with self-gravity.

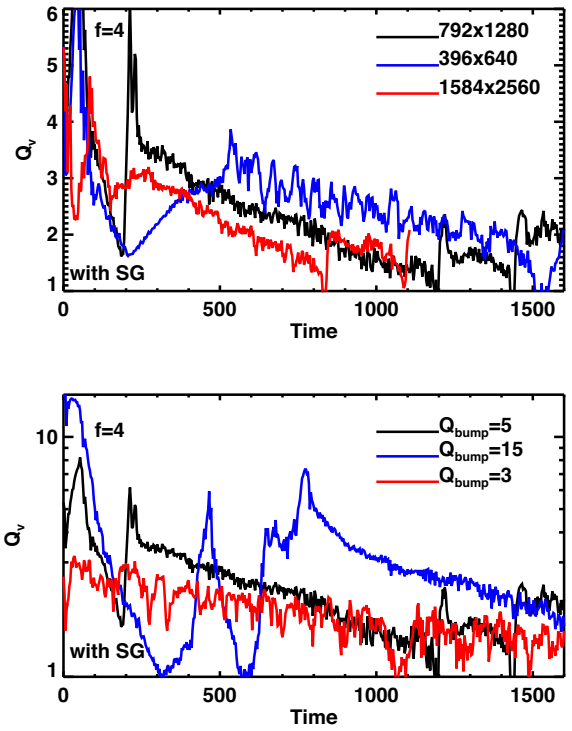

Figure 17. *Upper panel*: Time evolution of the Toomre parameter at vortex centre Q_v for the self-gravitating model with $f = 4$, and for different grid resolutions. *Lower panel:* Q_v as a function of time for the same run with our nominal grid resolution, but for different initial amplitudes for the density bump.

phases, but all ultimately resulted in vortex growth, with a very similar corresponding growth timescale.

We plot in the lower panel of Fig. 17 Q_v as a function of time for the same model and nominal grid resolution, but for runs which differ by the amplitude of the density bump at the end of the first step (see Section 2.2), and therefore by the initial value for the Toomre parameter $Q_{\rm bump}$ at the location of the pressure bump. The case $Q_{\rm bump} = 15$ corresponds to a situation where the initial amplitude of the density bump is zero, such that the vortex forms as soon as the density bump is strong enough for the RWI criterion to be satisfied. We see that the duration of the relaxation phase is longer in that case, but vortex collapse ultimately occurs, consistent with that found in our reference model and in the model with $Q_{\rm bump} = 3$.

ACKNOWLEDGEMENTS

We thank Z. Regály for useful discussions. Computer time for this study was provided by the computing facilities MCIA (Mésocentre de Calcul Intensif Aquitain) of the Universite de Bordeaux and by HPC resources of Cines under the allocation A0010406957 made by GENCI (Grand Equipement National de Calcul Intensif).

REFERENCES

Adams F. C., Ruden S. P., Shu F. H., 1989, ApJ, 347, 959
Ataiee S., Pinilla P., Zsom A., Dullemond C. P., Dominik C., Ghanbari J., 2013, A&A, 553, L3
Bae J., Hartmann L., Zhu Z., Nelson R. P., 2014, ApJ, 795, 61
Balbus S. A., Hawley J. F., 1991, ApJ, 376, 214
Baruteau C., Masset F., 2008, ApJ, 678, 483
Baruteau C., Meru F., Paardekooper S.-J., 2011, MNRAS, 416, 1971
Baruteau C., Papaloizou J. C. B., 2013, ApJ, 778, 7
Casassus S. et al., 2013, Nature, 493, 191
Chiang E., Laughlin G., 2013, MNRAS, 431, 3444
Cossou C., Raymond S. N., Hersant F., Pierens A., 2014, A&A, 569, A56
Crida A., Morbidelli A., Masset F., 2006, Icarus, 181, 587
de Val-Borro M. et al., 2006, MNRAS, 370, 529
D'Angelo G., Henning T., Kley W., 2003, ApJ, 599, 548
Faure J., Fromang S., Latter H., Meheut H., 2015, A&A, 573, A132
Flock M., Fromang S., Turner N. J., Benisty M., 2017, ApJ, 835, 230
Fukagawa M. et al., 2013, PASJ, 65, L14
Gammie C. F., 1996, ApJ, 457, 355
Gammie C. F., 2001, ApJ, 553, 174
Gressel O., Nelson R. P., Turner N. J., 2012, MNRAS, 422, 1140
Hansen B. M. S., Murray N., 2012, ApJ, 751, 158
Izidoro A., Ogihara M., Raymond S. N., Morbidelli A., Pierens A., Bitsch B., Cossou C., Hersant F., 2017, MNRAS, 470, 1750
Kley W., Dirksen G., 2006, A&A, 447, 369
Latter H. N., Balbus S., 2012, MNRAS, 424, 1977
Les R., Lin M.-K., 2015, MNRAS, 450, 1503
Lesur G., Papaloizou J. C. B., 2009, A&A, 498, 1
Li H., Colgate S. A., Wendroff B., Liska R., 2001, ApJ, 551, 874
Li H., Finn J. M., Lovelace R. V. E., Colgate S. A., 2000, ApJ, 533, 1023
Lin M.-K., 2012, MNRAS, 426, 3211
Lin M. K., Kratter K. M., 2016, ApJ, 824, 91
Lin M.-K., Papaloizou J. C. B., 2011, MNRAS, 415, 1426
Lin M.-K., Pierens A., 2018, MNRAS, 478, 575
Lissauer J. J. et al., 2011, ApJS, 197, 8
Lovelace R. V. E., Hohlfeld R. G., 2013, MNRAS, 429, 529
Lovelace R. V. E., Li H., Colgate S. A., Nelson A. F., 1999, ApJ, 513, 805
Lovis C. et al., 2011, A&A, 528, A112
Lyra W., Lin M. K., 2013, ApJ, 775, 17
Masset F., 2000, A&AS, 141, 165
Müller T. W. A., Kley W., Meru F., 2012, A&A, 541, A123
Ogihara M., Ida S., 2009, ApJ, 699, 824
Okuzumi S., Hirose S., 2011, ApJ, 742, 65
Paardekooper S.-J., Lesur G., Papaloizou J. C. B., 2010, ApJ, 725, 146
Papaloizou J. C. B., 2005, A&A, 432, 757
Pierens A., Baruteau C., Hersant F., 2011, A&A, 531, A5
Pierens A., Baruteau C., Hersant F., 2012, MNRAS, 427, 1562
Raymond S. N., Cossou C., 2014, MNRAS, 440, L11
Regály Z., Juhász A., Sándor Z., Dullemond C. P., 2012, MNRAS, 419, 1701
Regály Z., Vorobyov E., 2017, MNRAS, 471, 2204
Rein H., 2012, MNRAS, 427, L21
Richard S., Barge P., Le Dizès S., 2013, A&A, 559, A30
Shakura N. I., Sunyaev R. A., 1973, A&A, 24, 337
Terquem C., Papaloizou J. C. B., 2007, ApJ, 654, 1110
Umebayashi T., Nakano T., 1988, Prog. Theor. Phys. Suppl., 96, 151
van der Marel N. et al., 2013, Science, 340, 1199
van Leer B., 1977, J. Comput. Phys., 23, 276
Ward W. R., 1997, Icarus, 126, 261
Yellin-Bergovoy R., Heifetz E., Umurhan O. M., 2016, Geophys. Astrophys. Fluid Dyn., 110, 274
Zhu Z., Baruteau C., 2016, MNRAS, 458, 3918
Zhu Z., Hartmann L., Nelson R. P., Gammie C. F., 2012, ApJ, 746, 110
Zhu Z., Stone J. M., Rafikov R. R., Bai X.-n., 2014, ApJ, 785, 122

This paper has been typeset from a TEX/LATEX file prepared by the author.